Electrochemistry-based Battery Modeling for Prognostics

Matthew Daigle[1] and Chetan S. Kulkarni[2]

[1] *NASA Ames Research Center, Moffett Field, CA, 94035, USA*
matthew.j.daigle@nasa.gov

[2] *SGT, Inc., NASA Ames Research Center, Moffett Field, CA, 94035, USA*
chetan.s.kulkarni@nasa.gov

ABSTRACT

Batteries are used in a wide variety of applications. In recent years, they have become popular as a source of power for electric vehicles such as cars, unmanned aerial vehicles, and commericial passenger aircraft. In such application domains, it becomes crucial to both monitor battery health and performance and to predict end of discharge (EOD) and end of useful life (EOL) events. To implement such technologies, it is crucial to understand how batteries work and to capture that knowledge in the form of models that can be used by monitoring, diagnosis, and prognosis algorithms. In this work, we develop electrochemistry-based models of lithium-ion batteries that capture the significant electrochemical processes, are computationally efficient, capture the effects of aging, and are of suitable accuracy for reliable EOD prediction in a variety of usage profiles. This paper reports on the progress of such a model, with results demonstrating the model validity and accurate EOD predictions.

1. INTRODUCTION

With electric unmanned aerial vehicles, electric/hybrid cars, and commercial passenger aircraft, we are witnessing a drastic increase in the usage of batteries to power vehicles. These vehicles are being deployed in military, civilian and scientific applications all over the world. However, for battery-powered vehicles to operate at maximum efficiency and reliability, it becomes crucial to both monitor battery health and performance and to predict end of discharge (EOD) and end of useful life (EOL) events.

For example, NASA's Mars Global Surveyor stopped operating in late 2006 due to battery overheating caused by the raditor being oriented directly towards the sun, resulting in a significant loss of capacity (Saha & Goebel, 2009). Both the AFRL ARGOS satellite and the Viking 2 Mars Lander also suffered battery failures. More recently, problems have arisen in the Boeing Dreamliner aircraft, which utilize lithium-ion (Li-ion) batteries for auxiliary power (Ross, 2013). Battery monitoring failed to capture thermal runaway conditions, leading to fire. With advanced health monitoring and predictive capabilities, such problems can be prevented.

To implement such technologies, it is crucial to understand how batteries work and to capture that knowledge in the form of models that can be used by monitoring, diagnosis, and prognosis algorithms. Several battery modeling methodologies have been developed in the literature. The models can generally be classified as *empirical models*, *electrochemical engineering models*, *multi-physics models*, and *molecular/atomist models* (Ramadesigan et al., 2012). Emprical models (e.g., (Saha & Goebel, 2009)), are based on fitting certain functions to past experimental data, without making use of any physicochemical principles. Electrical circuit equivalent models are popular forms of empirical models, e.g., (Ceraolo, 2000; Chen & Rincon-Mora, 2006; Daigle, Saxena, & Goebel, 2012). Electrochemical engineering models are typically continuum models that include electrochemical kinetics and transport phenomena, e.g. (Karthikeyan, Sikha, & White, 2008; Rong & Pedram, 2006; Ning & Popov, 2004; Doyle, Fuller, & Newman, 1993; Newman & Tiedemann, 1975). The former type of model has the advantage of being computationally efficient, but the disadvantage of limited accuracy and robustness, due to the approximations in battery behavior that are made, and as a result of such approximations, cannot represent aging well. The latter type of model has the advantage of being very accurate, but are often computationally inefficient, having to solve complex sets of partial differential equations, and thus being ill-suited to online application of prognostics. Similarly, multi-physics (Lee, Smith, Pesaran, & Kim, 2013) and atomist models are even less suited to online application.

In this work, we develop an electrochemistry-based model of Li-ion batteries, that (*i*) capture the significant electrochemical processes, (*ii*) are computationally efficient, (*iii*) capture

Matthew Daigle et al. This is an open-access article distributed under the terms of the Creative Commons Attribution 3.0 United States License, which permits unrestricted use, distribution, and reproduction in any medium, provided the original author and source are credited.

the effects of aging, and (*iv*) are of suitable accuracy for reliable EOD prediction in a variety of usage profiles. The model can be considered an electrochemical engineering model, but unlike most such models found in the literature, we make certain approximations that allow us to retain computational efficiency. Although we focus here on Li-ion batteries, the model is quite general and can be applied to different chemistries through a change of model parameter values. This paper reports on the progress of such a model, providing model validation results and EOD prediction results.

The paper is organized as follows. Section 2 provides background material on batteries. Section 3 describes the model-based prognostics framework. Section 4 develops the electrochemistry-based battery model. Section 5 provides model validation and battery prognosis results. Section 6 concludes the paper.

2. BACKGROUND

A battery converts chemical energy into electrical energy, and often consists of many cells. A cell consists of a positive electrode and a negative electrode with electrolyte in which the ions can migrate. For Li-ion, a common chemistry is a positive electrode consisting of lithium cobalt oxide ($\mathrm{Li}_x\mathrm{CoO}_2$) and negative electrode of lithiated carbon ($\mathrm{Li}_x\mathrm{C}$). These active materials are bonded to metal-foil current collectors at both ends of the cell and electrically isolated by a microporous polymer separator film that is permeable to Li ions. The electrolyte enables lithium ions (Li^+) to diffuse between the positive and negative electrodes. The lithium ions insert or deinsert from the active material (known as intercalation and deintercalation) depending upon the electrode and whether the active process is charging or discharging.

A schematic of the battery during the discharge process is shown in Fig. 1. When fully charged, the active (mobile) Li ions reside in the negative electrode. Upon connecting a load to the battery, current is allowed to flow from the positive to the negative electrode. This is supported by the oxidation reaction (loss of electrons) in the negative electrode (acting as the anode):

$$\mathrm{Li}_x\mathrm{C} \xrightarrow{\text{discharge}} \mathrm{C} + x\mathrm{Li}^+ + x\mathrm{e}^-,$$

which results in the liberation of Li ions and electrons. The electrons move through the load from the negative to positive electrode, and the Li ions move in the same direction from the negative to the positive electrode through the separator. In the positive electrode (acting as the cathode), the reduction reaction (gain of electrons) takes place:

$$\mathrm{Li}_{1-x}\mathrm{CoO}_2 + x\mathrm{Li}^+ + x\mathrm{e}^- \xrightarrow{\text{discharge}} \mathrm{LiCoO}_2$$

During charging, a current source forces current to move from the negative to the positive electrode, as shown in Fig. 2. The active material in the positive electrode (acting as the anode) is oxidized and Li ions are de-intercalated with the corresponding reaction:

$$\mathrm{LiCoO}_2 \xrightarrow{\text{charge}} \mathrm{Li}_{1-x}\mathrm{CoO}_2 + x\mathrm{Li}^+ + x\mathrm{e}^-$$

that results in the loss of Li ions and electrons, which can then move to the negative electrode (acting as the cathode). The reduction reaction takes place in the negative electrode:

$$\mathrm{C} + x\mathrm{Li}^+ + x\mathrm{e}^- \xrightarrow{\text{charge}} \mathrm{Li}_x\mathrm{C}$$

Theoretically the cell has a voltage of around 4.2 V when fully charged. The terminal voltage of the battery rises/falls with a charge/discharge cycle, respectively. At the end of the charging/discharging period the battery voltage settles to a steady-state value that is a function of its state of charge (SOC). SOC is conventionally defined to be 1 when the battery is fully charged and 0 when the battery is fully discharged. Hence even in a degraded battery the SOC for max-

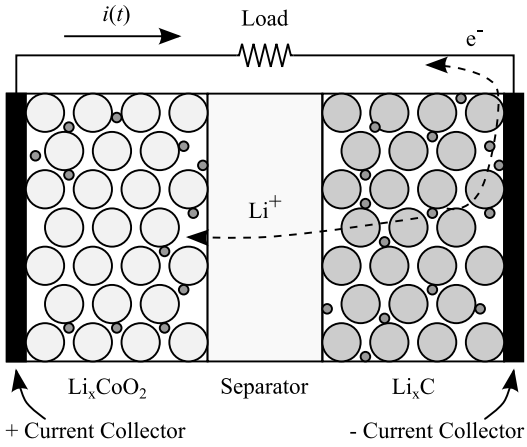

Figure 1. Li-ion battery during discharge.

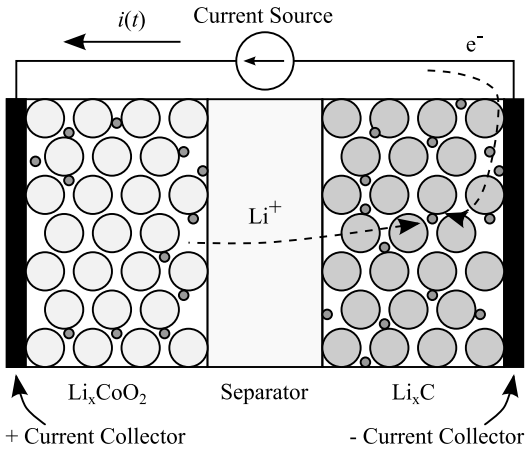

Figure 2. Li-ion battery during charge.

imum charge is always 1 by definition.

The charge/discharge dynamics of batteries can be characterized by taking voltage measurements under constant current charge/discharge conditions. The rate of charge/discharge is measured relative to the battery capacity C. For example, a $0.1C$ discharge rate for a 5 Ah battery is 0.5 A.

Charging typically consists of periods of constant current (CC) and/or constant voltage (CV) charging. At lower SOC, a CC charge is applied to bring the battery voltage to the CV level. Once the desired voltage level is achieved, the charger switches to CV mode and current decreases until 100% SOC is reached. The charger is not operated in CV mode at lower SOC levels since this will increase the amount of current flowing throught the battery while charging, leading to additional heat generation and side reactions taking place that may affect the battery life. The charge acceptance is the maximum permissible rate at which batteries can be charged. For Li-ion batteries the recommended charge acceptance is $C/3$.

The end of life of a battery depends on the chemistry, discharge-charge cycling, temperature, and storage conditions, among other factors. Atmospheric temperature affects the operating performance of the batteries. At low temperatures, ionic diffusion and migration could be hindered and also damaging side reactions like lithium plating may take place. High temperatures cause corrosion and generation of gases leading to an increase in internal pressure. As the battery ages, degradation results in the decrease in the observed battery capacity. This is primarily due to a loss of mobile ions due to parasitic or side reactions and an increase in the internal resistance. Internal resistance leads to ohmic losses that generate heat and accelerate the aging process. Some relevant physical aging mechanisms in the electrodes are:

1. Solid-electrolyte interface (SEI) layer growth: The negative electrode degrades with the growth of the SEI layer leading to an increase in the impedance. The layers are formed during cycling and storage at high temperatures and entrains the lithium.
2. Lithium corrosion: Lithium in the active carbon material of the negative electrode corrodes over time leading to degradation. This causes a decrease in the capacity due to irreversible loss of mobile lithium ions.
3. Lithium plating: At low temperatures, high charge rates and low cell voltages forms a plating layer on the negative electrode which leads to irreversible loss of lithium.
4. Contact loss: SEI layer disconnects from the negative electrode which leads to contact loss and an increase in impedance.

3. BATTERY PROGNOSTICS

In this section we describe the general model-based prognostics problem and an implementation architecture, and describe how it applies to batteries.

3.1. Problem Formulation

We assume the system model may be generally defined as

$$\mathbf{x}(k+1) = \mathbf{f}(k, \mathbf{x}(k), \boldsymbol{\theta}(k), \mathbf{u}(k), \mathbf{v}(k)), \tag{1}$$

$$\mathbf{y}(k) = \mathbf{h}(k, \mathbf{x}(k), \boldsymbol{\theta}(k), \mathbf{u}(k), \mathbf{n}(k)), \tag{2}$$

where k is the discrete time variable, $\mathbf{x}(k) \in \mathbb{R}^{n_x}$ is the state vector, $\boldsymbol{\theta}(k) \in \mathbb{R}^{n_\theta}$ is the unknown parameter vector, $\mathbf{u}(k) \in \mathbb{R}^{n_u}$ is the input vector, $\mathbf{v}(k) \in \mathbb{R}^{n_v}$ is the process noise vector, $\mathbf{f}$ is the state equation, $\mathbf{y}(k) \in \mathbb{R}^{n_y}$ is the output vector, $\mathbf{n}(k) \in \mathbb{R}^{n_n}$ is the measurement noise vector, and $\mathbf{h}$ is the output equation.[1]

In prognostics, we are interested in predicting the occurrence of some event E that is defined with respect to the states, parameters, and inputs of the system. We define the event as the earliest instant that some event threshold $T_E : \mathbb{R}^{n_x} \times \mathbb{R}^{n_\theta} \times \mathbb{R}^{n_u} \to \mathbb{B}$, where $\mathbb{B} \triangleq \{0, 1\}$ changes from the value 0 to 1. That is, the time of the event k_E at some time of prediction k_P is defined as

$$k_E(k_P) \triangleq \inf\{k \in \mathbb{N} \colon k \geq k_P \wedge T_E(\mathbf{x}(k), \boldsymbol{\theta}(k), \mathbf{u}(k)) = 1\}. \tag{3}$$

The time remaining until that event, Δk_E, is defined as

$$\Delta k_E(k_P) \triangleq k_E(k_P) - k_P. \tag{4}$$

In the context of systems health management, T_E is defined via a set of performance constraints that define what the acceptable states of the system are, based on $\mathbf{x}(k)$, $\boldsymbol{\theta}(k)$, and $\mathbf{u}(k)$ (Daigle & Goebel, 2013). For batteries, there are two types of predictions that we are interested in. The first is EOD, defined by a voltage threshold V_{EOD}. In this case, T_E is defined by $V < V_{EOD}$, that is, when the battery voltage is less than the cutoff voltage, EOD is reached and T_E evaluates to 1. The second type of prediction is EOL, which is typically defined by a lower bound on the effective battery capacity (Saha & Goebel, 2009). In this case, T_E is defined by $C < C_{EOL}$, where C is the measured battery capacity and C_{EOL} is the lower bound on capacity.

3.2. Prognostics Architecture

We adopt a model-based prognostics architecture (Daigle & Goebel, 2013), in which there are two sequential problems, (*i*) the *estimation* problem, which requires determining a joint state-parameter estimate $p(\mathbf{x}(k), \boldsymbol{\theta}(k) | \mathbf{y}(k_0{:}k))$ based on the history of observations up to time k, $\mathbf{y}(k_0{:}k)$, and (*ii*) the *prediction* problem, which determines at k_P, using $p(\mathbf{x}(k), \boldsymbol{\theta}(k) | \mathbf{y}(k_0{:}k))$, a probability distribution

[1] Here, we use bold typeface to denote vectors, and use n_a to denote the length of a vector $\mathbf{a}$.

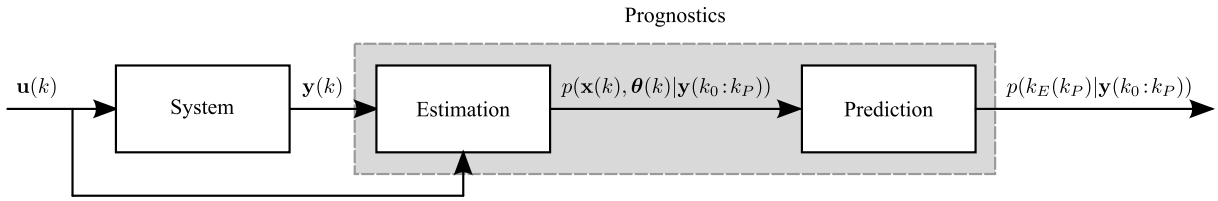

Figure 3. Prognostics architecture.

$p(k_E(k_P)|\mathbf{y}(k_0{:}k_P))$. The distribution for Δk_E can be trivially computed from $p(k_E(k_P)|\mathbf{y}(k_0{:}k_P))$ by subtracting k_P. Both steps require a dynamic model in the form of equations 1 and 2.

The prognostics architecture is shown in Fig. 3. In discrete time k, the system is provided with inputs $\mathbf{u}_k$ and provides measured outputs $\mathbf{y}_k$. The estimation module uses this information, along with the system model, to compute an estimate $p(\mathbf{x}(k), \boldsymbol{\theta}(k)|\mathbf{y}(k_0{:}k))$. The prediction module uses the joint state-parameter distribution and the system model, along with hypothesized future inputs, to compute the probability distribution $p(k_E(k_P)|\mathbf{y}(k_0{:}k_P))$ at given prediction times k_P.

In the application of prognostics in this example, we do not account for any uncertainty except for that provided in the state estimate, as our focus is on determining how accurate the model can predict EOD given precise information about the future. A more general prognostics architecure that accounts for these additional sources of uncertainty is described in (Daigle, Saxena, & Goebel, 2012; Sankararaman, Daigle, Saxena, & Goebel, 2013).

4. Battery Modeling

In order to predict end-of-discharge as defined by a voltage cutoff, the battery model must compute the voltage as a function of time given the current drawn from the battery. There are several electrochemical processes that contribute to the cell's potential that make this a difficult problem. We focus here on a lumped-parameter ordinary differential equations form, so it is efficient and usable for on-line prognostics, yet still considers the main electrochemical processes. We focus here specifically on Li-ion 18650 batteries with an average nominal voltage of 3.7V and nominal capacity of 2200mAh, however, the model is still general enough that with some modifications it may be applied to different battery chemistries.

The voltages of a battery are summarized in Fig. 4 (adapted from (Rahn & Wang, 2013)). The overall battery voltage $V(t)$ is the difference between the potential at the positive current collector, $\phi_s(0,t)$, and the negative current collector, $\phi_s(L,t)$, minus resistance losses at the current collectors (not shown in the diagram). As shown in the figure, the potentials vary with the distance $d \in [0, L]$, because the loss varies with distance from the current collectors.

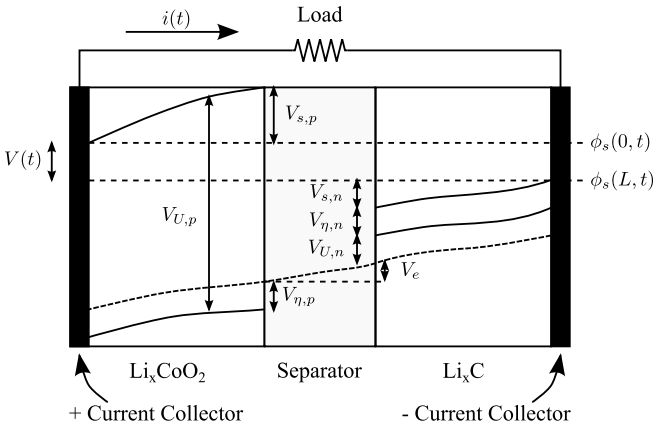

Figure 4. Battery voltages.

The potentials at the current collectors are described by several voltage terms. At the positive current collector is the equilibrium potential $V_{U,p}$. This voltage is then reduced by $V_{s,p}$, due to the solid-phase ohmic resistance, and $V_{\eta,p}$, the surface overpotential. The electrolyte ohmic resistance then causes another drop V_e. At the negative electrode, there is a drop $V_{\eta,n}$ due to the surface overpotential, and a drop $V_{s,n}$ due to the solid-phase resistance. The voltage drops again due to the equilibrium potential at the negative current collector $V_{U,n}$. We describe each of these voltage terms in turn.

4.1. Equilibrium Potential

In an ideal battery, the equilibrium potential of an electrode is described by the Nernst equation:

$$V_{U,i} = U_0 + \frac{RT}{nF} \ln\left(\frac{\gamma_{\beta,i} x_{\beta,i}}{\gamma_{\alpha,i} x_{\alpha,i}}\right), \tag{5}$$

or, equivalently,

$$V_{U,i} = U_0 + \frac{RT}{nF} \ln\left(\frac{x_{\beta,i}}{x_{\alpha,i}}\right) + \frac{RT}{nF} \ln\left(\frac{\gamma_{\beta,i}}{\gamma_{\alpha,i}}\right), \tag{6}$$

where i refers to the electrode (n for negative or p for positive), U_0 is a reference potential, R is the universal gas constant, T is the electrode temperature, n is the number of electrons transferred in the reaction ($n = 1$ for Li-ion), F is Faraday's constant, x is the mole fraction, where α refers to the lithium-intercalated host material and β to the unoccupied

host material, and γ is the activity coefficient (Karthikeyan et al., 2008). When discharging, Li ions move out of the negative electrode and into the positive electrode, so $x_{\alpha,n}$ and $x_{\beta,p}$ decrease while $x_{\beta,n}$ and $x_{\alpha,p}$ increase. As a result, $V_{U,p} - V_{U,n}$ will decrease. In an ideal condition the activity coefficients are unity and so the last term disappears, resulting in the classical form of the Nernst equation.

In the case of a Li-ion battery, $x_{\beta,i} = 1 - x_{\alpha,i}$, so we can rewrite the equation making this substitution. We then define x_i as $x_{\alpha,i}$ and drop the α subscript:

$$V_{U,i} = U_0 + \frac{RT}{nF} \ln\left(\frac{1 - x_i}{x_i}\right) + V_{\text{INT},i}, \tag{7}$$

where $V_{\text{INT},i}$ is the activity correction term (0 in the ideal condition). For Li_xCoO_2, x must be at least 0.4; Li cannot be reversibly removed beyond that (Karthikeyan et al., 2008).

We let q_i represent the amount of Li ions in electrode i, as measured in Coulombs. Recall that the flow of Li ions moves opposite to the flow of current. Therefore q_i changes in the same direction as x_i, and we may define x_i based on q_i using

$$x_i = \frac{q_i}{q^{\max}}, \tag{8}$$

where $q^{\max} = q_p + q_n$ refers to the total amount of available (i.e., mobile) Li ions. It follows then that $x_p + x_n = 1$. When fully charged, $x_p = 0.4$ and $x_n = 0.6$. When fully discharged, $x_p = 1$ and $x_n = 0$.

Batteries are nonideal and therefore the assumption of unity activity coefficients is not applicable. As a result, battery models often resort to curve-fitting for modeling the equilibrium potential. The equilibrium potential can be obtained by discharging the battery at a very slow rate, such that a concentration gradient will not build up, temperature is steady, and voltage drops due to internal resistances and other overpotentials are negligible. Fig. 5 shows the measured voltage ($V_{U,p} - V_{U,n}$) as a function of mole fraction against that predicted by the Nernst equation. Clearly, the Nernst equation cannot fit this case so it must be nonideal.

The activity coefficient terms are related to excess Gibbs free energy and can be captured using the Redlich-Kister expansion (Karthikeyan et al., 2008). We then have

$$V_{\text{INT},i} = \frac{RT}{nF} \ln\left(\frac{\gamma_{\beta,i}}{\gamma_{\alpha,i}}\right) \tag{9}$$

$$= \frac{1}{nF}\left(\sum_{k=0}^{N_i} A_{i,k}\left((2x_i - 1)^{k+1} - \frac{2x_i k(1 - x_i)}{(2x_i - 1)^{1-k}}\right)\right). \tag{10}$$

The number of terms N_i in the above expansion and the fitting parameters $A_{i,k}$ must be identified. Fig. 6 shows the modified equation fitted to the measured equilibrium potential for

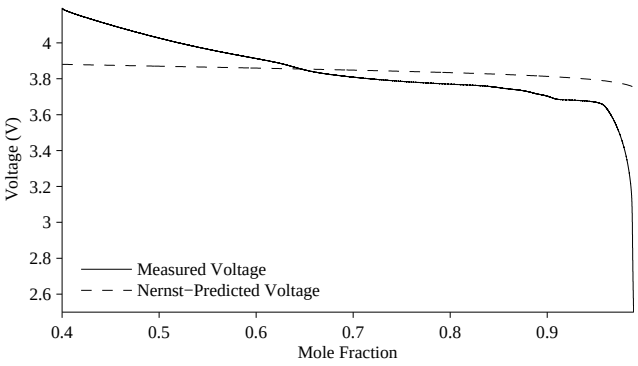

Figure 5. Measured and Nernst-predicted open-circuit potential.

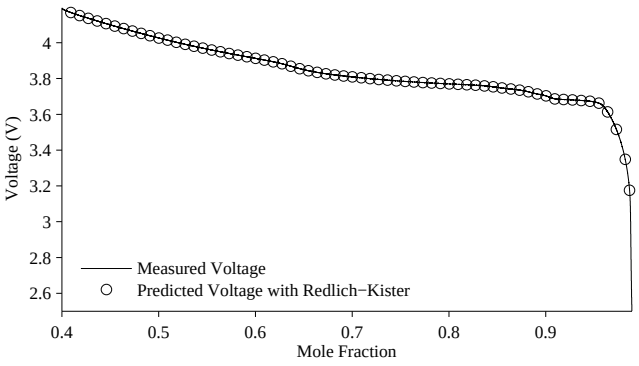

Figure 6. Measured and Redlich-Kister-predicted open-circuit potential.

$N_p = 12$ and $N_n = 0$. Clearly, the modified equation much more realistically reflects the true voltage curve. The identified parameters are given in Table 1 and were determined using the Nelder-Mead simplex method. The identified parameters represent those achieving a least-squares (local) error minimum, which is satisfactory for our purposes.

4.2. Concentration Overpotential

When a battery is discharged, the reactions take place at the surface of the electrode and this results in a concentration gradient. The concept is shown in Fig. 7. In the bulk volume, the concentration is nearly even, but close to the electrode the concentration changes drastically. To accommodate this, one may split the total volume into two individual control volumes (CVs), one for the bulk (with subscript b) and one for the surface (with subscript s).

For the volumes, the concentration of Li ions is computed as

$$c_{b,i} = \frac{q_{b,i}}{v_{b,i}} \tag{11}$$

$$c_{s,i} = \frac{q_{s,i}}{v_{s,i}}, \tag{12}$$

Table 1. Battery Model Parameters

Parameter	Value
$U_{0,p}$	4.03 V
$A_{p,0}$	−33642.23 J/mol
$A_{p,1}$	0.11 J/mol
$A_{p,2}$	23506.89 J/mol
$A_{p,3}$	−74679.26 J/mol
$A_{p,4}$	14359.34 J/mol
$A_{p,5}$	307849.79 J/mol
$A_{p,6}$	85053.13 J/mol
$A_{p,7}$	−1075148.06 J/mol
$A_{p,8}$	2173.62 J/mol
$A_{p,9}$	991586.68 J/mol
$A_{p,10}$	283423.47 J/mol
$A_{p,11}$	−163020.34 J/mol
$A_{p,12}$	−470297.35 J/mol
$U_{0,n}$	0.01 V
$A_{n,0}$	86.19 J/mol

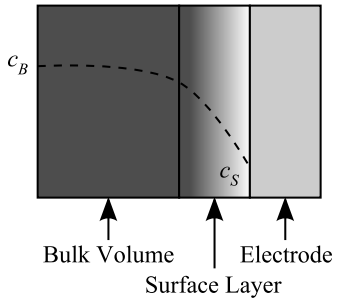

Figure 7. Concentration gradient.

where, for CV v in electrode i, $c_{v,i}$ is the concentration and $v_{v,i}$ is the volume. We define $v_i = v_{b,i} + v_{s,i}$. Note now that the following relations hold:

$$q_p = q_{s,p} + q_{b,p} \tag{13}$$
$$q_n = q_{s,n} + q_{b,n} \tag{14}$$
$$q^{\max} = q_{s,p} + q_{b,p} + q_{s,n} + q_{b,n}. \tag{15}$$

As the battery discharges, Li ions must move out of the surface layer at the negative electrode, through the bulk, and to the surface layer at the positive electrode, in order to match the flow of electrons. Li ions also move from the bulk CV to the surface due to the concentration gradient. The diffusion rate from the bulk to the surface is expressed as

$$\dot{q}_{bs,i} = \frac{1}{D}(c_{b,i} - c_{s,i}), \tag{16}$$

where D is the diffusion constant.

The q variables are described as

$$\dot{q}_{s,p} = i_{app} + \dot{q}_{bs,p} \tag{17}$$
$$\dot{q}_{b,p} = -\dot{q}_{bs,p} + i_{app} - i_{app} \tag{18}$$
$$\dot{q}_{b,n} = -\dot{q}_{bs,n} + i_{app} - i_{app} \tag{19}$$
$$\dot{q}_{s,n} = -i_{app} + \dot{q}_{bs,n}, \tag{20}$$

where i_{app} is the applied electric current. Initially, $c_{s,i} = c_{b,i}$ and so diffusion is zero. Once discharge begins, ions move from the surface layer of the negative electrode to the bulk volume of the negative electrode, through the separator to the bulk volume of the positive electrode and then on to the surface layer of the positive electrode. If the applied current is larger than the diffusion rate, then a concentration gradient will build up between the surface and bulk volumes. Once discharge stops, then only diffusion is active, and the concentrations will even out, causing a rise in voltage (because the concentration lowers in the surface layer of the positive electrode, raising the voltage, and the concentration rises in the surface layer of the negative electrode, raising the voltage).

The concentration overpotential is the difference in voltage between the two CVs due to the difference in concentration. Using the expression for equilibrium potential, we can compute the potential for the bulk volume and the potential for the surface layer; the difference between them is the concentration overpotential. We can explicitly account for the concentration overpotential simply by using as the expression for equilibrium potential, the equilibrium potential of the surface layer, i.e.,

$$V_{U,i} = U_0 + \frac{RT}{nF} \ln\left(\frac{1 - x_{s,i}}{x_{s,i}}\right) + V_{\text{INT},i}, \tag{21}$$

where $x_{s,i}$ is computed using

$$x_{s,i} = \frac{q_{s,i}}{q_{s,i}^{\max}}, \tag{22}$$

and

$$q_{s,i}^{\max} = q^{\max}\frac{v_{s,i}}{v_i} \tag{23}$$

The mole fraction in the surface changes faster than the mole fraction at the bulk, causing a larger concentration gradient for larger applied current and smaller diffusion rates. The observed voltage depends only on what is happening in the surface layer, not the bulk. When discharge stops, the surface layer becomes like the bulk, accounting for the recovery in voltage. The battery may then be discharged further since the surface layers were replenished with ions (from the bulk) in the negative electrode.

4.3. Ohmic Overpotential

The voltage drops due to the solid-phase ohmic resistances, the electrolyte ohmic resistance, and the resistances at the current collectors can be treated as constant resistances and lumped together:

$$V_o = V_{s,p} + V_{s,n} + V_e + V_{cc,p} + V_{cc,n} \quad (24)$$
$$= i_{app}(R_{s,p} + R_{s,n} + R_e + R_{cc,p} + R_{cc,n}) \quad (25)$$
$$= i_{app}R_o, \quad (26)$$

where V_{cc} is the voltage drop over the current collectors, $R_{cc,i}$ is the resistance at the current collector for electrode i.

4.4. Surface Overpotential

The overpotentials due to charge transfer resistance and SEI kinetics are described by the Butler-Volmer equation. For small currents the overpotential is linear with current and for larger currents it is proportional to the log of the current, and these two characteristics are combined in the Butler-Volmer equation. The equation is given as

$$J_i = J_{i0}\left(\exp\left(\frac{(1-\alpha)F}{RT}V_{\eta,i}\right) - \exp\left(-\frac{\alpha F}{RT}V_{\eta,i}\right)\right), \quad (27)$$

where α is the symmetry factor, J_i is the current density, and J_{i0} is the exchange current density. The current densities are defined as

$$J_i = \frac{i}{S_i} \quad (28)$$
$$J_{i0} = k_i(1 - x_{s,i})^{\alpha}(x_{s,i})^{1-\alpha}, \quad (29)$$

where k_i is a lumped parameter of several constants including a rate coefficient, electrolyte concentration, and maximum ion concentration. The voltage drop takes place at the electrode surface, so $x_{s,i}$ is used in computing the exchange current density.

In the case of Li ions, the symmetry factor is 0.5, so the Butler-Volmer equation can be simplified and written in terms of voltage as

$$V_{\eta,i} = \frac{RT}{F\alpha}\text{arcsinh}\left(\frac{J_i}{2J_{i0}}\right). \quad (30)$$

4.5. State of Charge

As discussed in Section 2, the SOC of a battery is conventionally defined to be 1 when the battery is fully charged and 0 when the battery is fully discharged. In this model, it is analogous to the mole fraction x_n, but scaled from 0 to 1. There is a difference here between nominal SOC and *apparent* SOC. Nominal SOC would be computed based on the combination of the bulk and surface layer CVs in the negative electrode, whereas apparent SOC would be computed based only on the surface layer. That is, a battery can be discharged at a given rate, and reach the voltage cutoff, i.e., apparent SOC is then 0. But, once the concentration gradient settles out, the surface layer will be partially replenished and the battery can be discharged further, i.e, apparent SOC increases whereas nominal SOC remains the same.

Nominal (n) and apparent (a) SOC can then be defined using

$$SOC_n = \frac{q_n}{0.6q^{\max}} \quad (31)$$
$$SOC_a = \frac{q_{s,n}}{0.6q^{\max_{s,n}}}, \quad (32)$$

where $q^{\max_{s,n}} = q^{\max}\frac{v_{s,n}}{v_n}$. The factor $1/0.6$ comes from the fact that the mole fraction at the positive electrode cannot go below 0.4 (as described in Section 4.1), therefore SOC of 1 corresponds to the point where $q_n = 0.6q^{\max_{s,n}}$.

4.6. Battery Voltage

Now that each of the voltage drops in Fig. 4 have been defined, battery voltage can be expressed as follows.

$$V = V_{U,p} - V_{U,n} - V_o - V_{\eta,p} - V_{\eta,n}. \quad (33)$$

Voltages in the battery are not observed to change instantaneously, i.e., the voltage changes occur smoothly. When discharge completes, for example, the voltage rises slowly as the surface layers move to the concentrations of the bulk volumes, as caused by diffusion. In addition to this, there are transients associated with V_o and the $V_{\eta,i}$ terms. To take this into account in a simple way, we compute voltage using

$$V = V_{U,p} - V_{U,n} - V'_o - V'_{\eta,p} - V'_{\eta,n}, \quad (34)$$

where

$$\dot{V}'_o = (V_o - V'_o)/\tau_o \quad (35)$$
$$\dot{V}'_{\eta,p} = (V_{\eta,p} - V'_{\eta,p})/\tau_{\eta,p} \quad (36)$$
$$\dot{V}'_{\eta,n} = (V_{\eta,n} - V'_{\eta,n})/\tau_{\eta,n}, \quad (37)$$

where the τ parameters are empirical time constants.

The model contains as states $\mathbf{x}$, $q_{s,p}$, $q_{b,p}$, $q_{b,n}$, $q_{s,n}$, V'_o, $V'_{\eta,p}$, and $V'_{\eta,n}$. The single model output is V.

Identified model parameters are given in Table 2. Some parameters are defined by the battery dimensions and chemistry. The remaining parameters are estimated based on data, as with the parameters in Table 1.

The measured and predicted discharge curves for a constant 2 A discharge are shown in Fig. 8. The model fits very well to the measured values. The accuracy towards the end of discharge is most sensitive to the Redlich-Kister parameters, the diffusion constant, and the volume of the surface layer. The

Table 2. Battery Model Parameters

Parameter	Value
$q^{\max}$	1.32×10^4 C
R	8.314 J/mol/K
T	292 K
F	96487 C/mol
n	1
D	7.0×10^6 mol s/C/m^3
τ_o	10 s
α	0.5
R_o	0.085 Ω
S_p	2×10^{-4} m^2
k_p	2×10^4 A/m^2
$v_{s,p}$	2×10^{-6} m^3
$v_{b,p}$	2×10^{-5} m^3
$\tau_{\eta,p}$	90 s
S_n	2×10^{-4} m^2
k_n	2×10^4 A/m^2
$v_{s,n}$	2×10^{-6} m^3
$v_{b,n}$	2×10^{-5} m^3
$\tau_{\eta,n}$	90 s

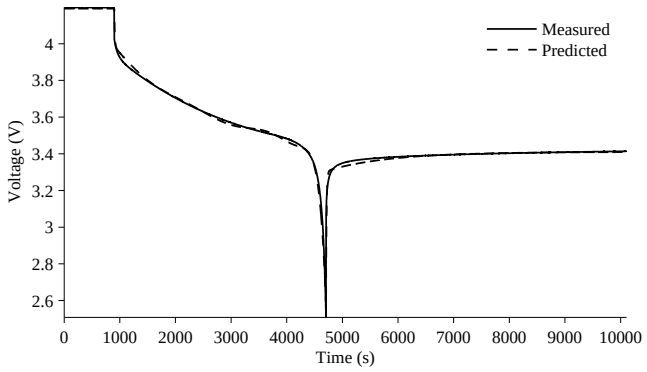

Figure 8. Measured and predicted 2 A discharge curves.

predicted end-of-discharge time can be finely tuned most easily by adjusting the time at which the amount of Li ions in the surface layer of the negative electrode hits zero and the surface layer of the postive electrode becomes full, because this is when the equilibrium voltage of these layers nears a combined 2.5 V. This is accomplished by adjusting the diffusion constant.

Model validation for a variable loading scenario is shown in Fig. 9. As shown in Fig. 9a, the load changes every 2 minutes, resulting in corresponding changes in voltage. Fig. 9b shows that the voltage predictions are fairly accurate in response to changes in load. Some errors are still present that may possibly be accounted for by including temperature effects.

4.7. Battery Aging

As described in Section 2, battery aging manifests in two major ways. The first is a loss of capacity due to parasitic and

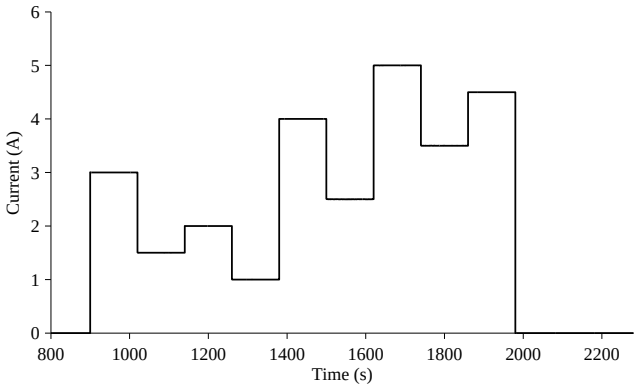

(a) Current.

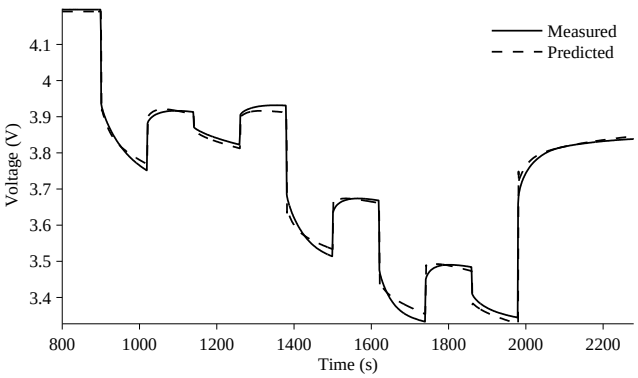

(b) Measured and predicted variable loading discharge curves.

Figure 9. Model validation for variable loading.

side reactions that result in a loss of active (mobile) Li ions. The second is an increase in internal resistance due to SEI layer growth and other factors. Capacity is typically measured with respect to a reference current and the associated EOD point as defined by a voltage cutoff. A decreased capacity will result in the voltage hitting the cutoff earlier. An increase in resistance will lower the voltage overall, so also result in hitting the cutoff earler. Therefore both these aging mechanisms result in a loss of measured capacity.

Fig. 10 shows 2 A discharge curves with the battery at different ages. The arrows in the figure illustrate the direction the curves move as the battery ages. The EOD point moves earlier in time due to diminished capacity. The voltage drops down during discharge due to increased resistance. Steady-state voltage after discharge increases because the battery is not discharged as fully due to the increased resistance and the battery reaching EOD before then.

In the battery model, the total available charge in the battery is represented through $q^{\max}$. Therefore, the loss of active material can be represented in the model through a change in $q^{\max}$. Fig. 11a shows how the discharge curve changes as $q^{\max}$ is decreased by 1% with each new discharge. We can see a slight decrease in voltage, which is due to the Butler-Volmer term,

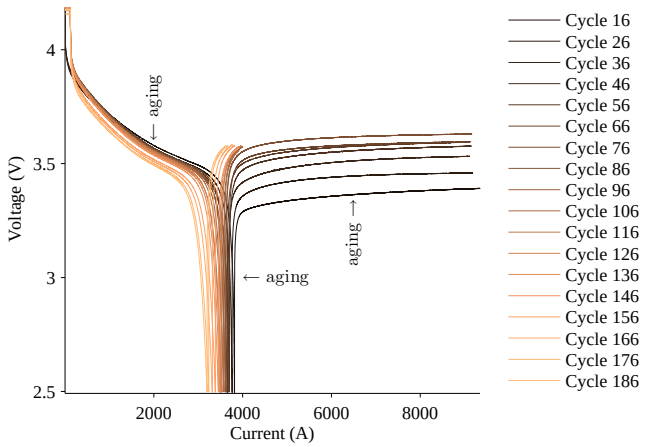

Figure 10. Measured 2 A discharge curves with battery aging.

which is dependent on mole fraction that is computed using $q^{\max}$. The EOD point moves earlier due to the discharge point being reached with less charge extracted. Steady-state voltage after discharge increases since the cutoff is reached with less relative charge extracted.

One way to validate this is by looking at the equilbrium potential plots as the battery ages, because the resistances are negligible. Fig. 12 shows the measured equilibrium potential of the battery ($V_{U,p} - V_{U,n}$) after 10 discharge cycles and after 30 discharge cycles. The curves are exactly the same, only the time scale changes; there is a 20 minute difference in EOD. Since equilibrium potential is a function only of mole fraction, and mole fraction is computed as $q/q^{\max}$, then decreasing $q^{\max}$ would change the time scale in this way.

Increase in internal resistance can be captured through an increase in the R_o parameter. Fig. 11b shows how the discharge curve changes as R_o is increased by 5% with each new discharge. The voltage drops, but the change in EOD is not significant, because the dynamics near EOD are dominated mainly by the equilibrium potential contribution with some contribution from the Butler-Volmer dynamics. The change in charge extracted is thereby also not significant so changes in steady-state voltage after discharge are very small.

From Figs. 11a and 11b, it is clear that changes in both $q^{\max}$ and R_o are required to capture how the discharge curve changes with aging. Fig. 11c shows the combined effects, with $q^{\max}$ decreasing by 1% and R_o increasing by 5% with each new discharge. The qualitative changes observed in Fig. 10 are now reproduced.

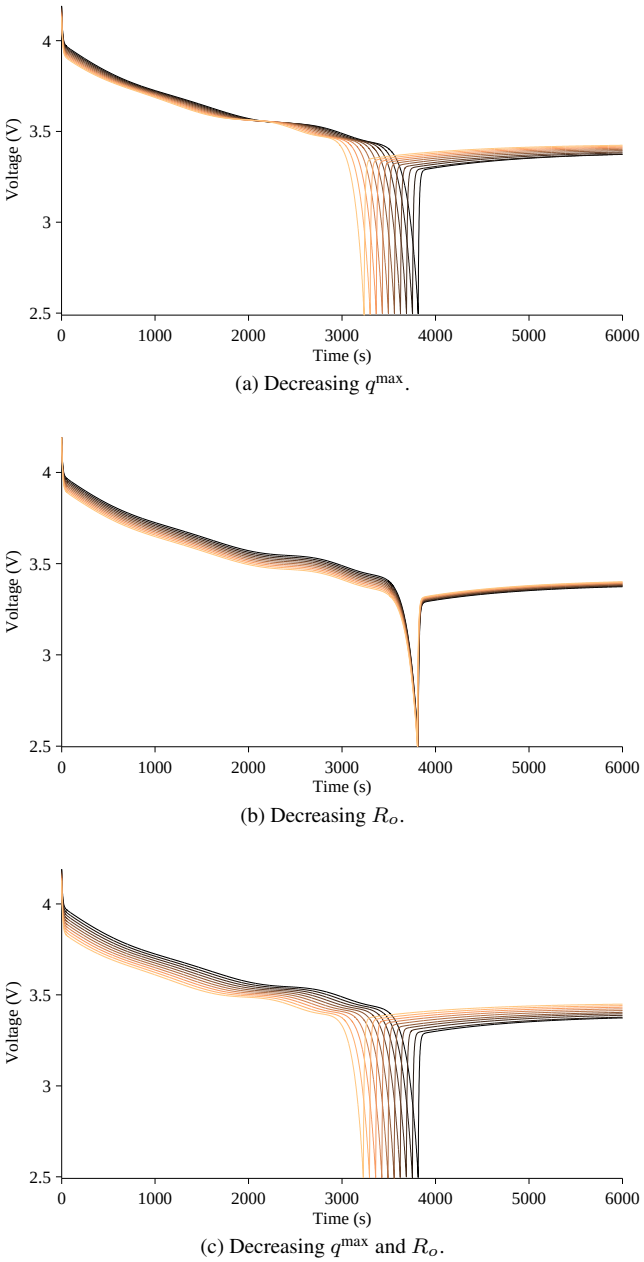

(a) Decreasing $q^{\max}$.

(b) Decreasing R_o.

(c) Decreasing $q^{\max}$ and R_o.

Figure 11. Simulated 2 A discharge curves with aging. Curves for later cycles are shown in lighter colors.

5. Application to Prognostics

With an accurate model and known future inputs to a system, prognostics should in turn be very accurate. In this section we demonstrate battery prognostics with the new model developed in this paper. We use the architecture described in Section 3. As an estimation algorithm, we use the unscented Kalman filter (UKF) with the battery model; see (Julier & Uhlmann, 1997, 2004) for details on the filter and (Daigle, Saha, & Goebel, 2012; Daigle, Saxena, & Goebel, 2012) for its application to prognostics. The UKF operates on a set of determinstically selected samples, called *sigma points*, that are used to represent the joint state-parameter distribution $p(\mathbf{x}(k), \boldsymbol{\theta}(k)|\mathbf{y}(k_0{:}k))$.

For the prediction algorithm, we perform a simple simulation

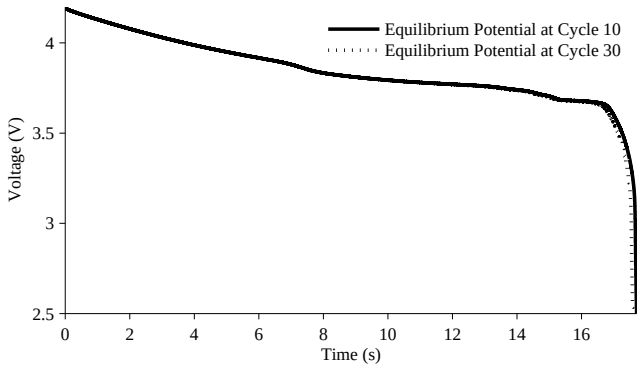

Figure 12. Shifting of equilibrium potentials due to aging.

as described in (Daigle & Goebel, 2013). Each sigma point is simulated forward using the model until EOD is reached; from the corresponding EODs for each sigma point we can construct the EOD distribution. In this work, we assume that the future inputs (i_{app}) are known, so the only uncertainty present in the prediction is that related to the model. We use $V_{\text{EOD}} = 2.6\ V$ as the voltage cutoff defining EOD.

As performance metrics, we use percent root mean square error (PRMSE) for estimation accuracy, and for prediction we use relative accuracy (RA) and relative standard deviation (RSD). We plot results in α-λ plots, where α (e.g. 10%) defines an accuracy cone around the ground truth, and λ is a time point (Saxena, Celaya, Saha, Saha, & Goebel, 2010).

Fig. 13 shows prognosis results from a 2 A discharge, assuming the future inputs (i_{app}) are known. As shown in Fig. 13a, the UKF tracks very well the measured voltage, since the underlying model is very accurate. Prediction results are, in turn, also very accurate and with very little uncertainty (the only uncertainty is related to the state estimation uncertainty), as shown in Fig. 13b. Overall, RA averages over all prediction points (every 100 s) to 99.38%, and RSD to 0.75%. Since the spread is so small, the 5%–25% and 75%–95% ranges cannot be seen on the plot.

Fig. 14 shows prognosis results from a 3 A discharge. In the open loop, the model slightly underestimates EOD, as shown in Fig. 14b. Even though the UKF tracks well, once a prediction is made the model is in the open loop, and since the model predicts an earlier EOD for the given load there is a bias in the predictions. The UKF helps keep the state estimate accurate and so reduces the error compared to using the model itself.

Fig. 15 shows prognosis results from a variable loading discharge, with EOD being defined in this case as 3.35 V. In the open loop, the model slightly overestimates EOD, as shown in Fig. 15b. The UKF tracks well and corrects for some of the model errors (see Fig. 9b). The model is more accurate at predicting EOD when defined towards the end of a discharge rather than in the middle of a discharge, so if the voltage threshold is defined to be higher, the predictions will be less accurate. In this case RA averages to 88.41%, and RSD to 2.13%. RSD is larger because the UKF needs to account for the additional model uncertainty since the model is less accurate in variable-loading scenarios.

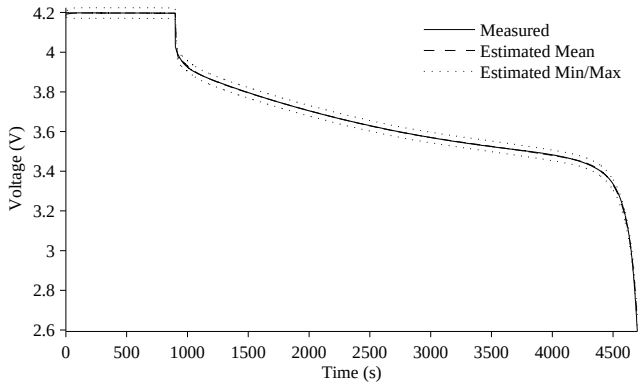

(a) Voltage estimation.

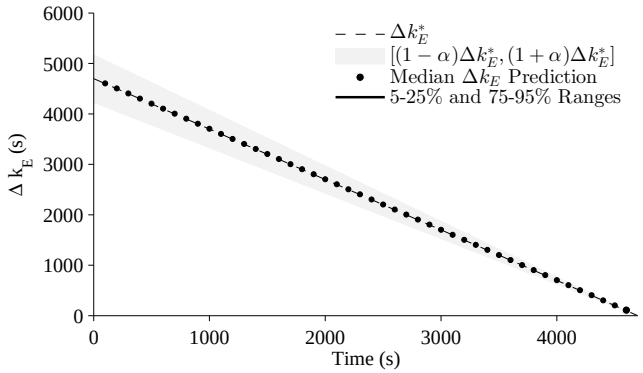

(b) EOD prediction

Figure 13. Prognostics results for 2 A discharge.

Additional results are shown in Table 3. PRMSE is very low as the UKF is able to track the voltage well in all cases. The predictions are also very accurate, with average RA above 90%, and precise, with RSD around 1% or lower. Although overall very good, the results are best around the 2 A discharge, suggesting that further model improvements (e.g., including temperature effects) may be necessary.

It is also worth mentioning that the model is not computationally intensive. The model is implemented with a fixed-step discrete-time simulation with a step size of 1 s. It takes on the order of 1×10^{-4} s to simulate 1 s of real time.

6. Conclusions

In this paper, we presented a new model for battery prognostics based on the underlying physics. Using equations based in electrochemistry, we developed a model that is both accu-

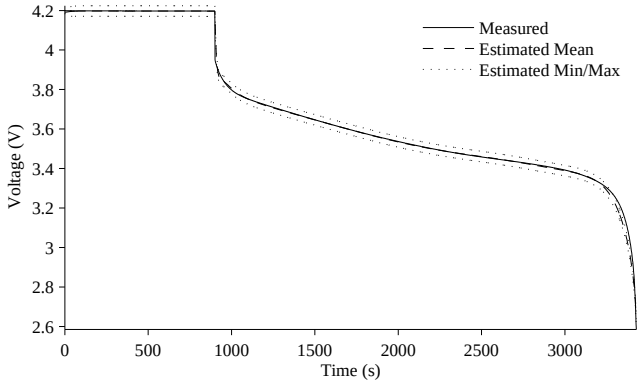

(a) Voltage estimation.

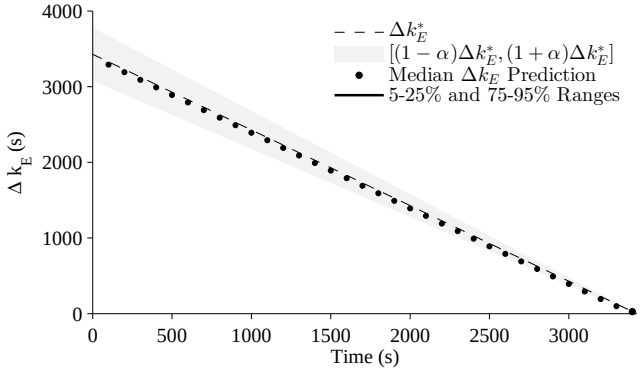

(b) EOD prediction

Figure 14. Prognostics results for 3 A discharge.

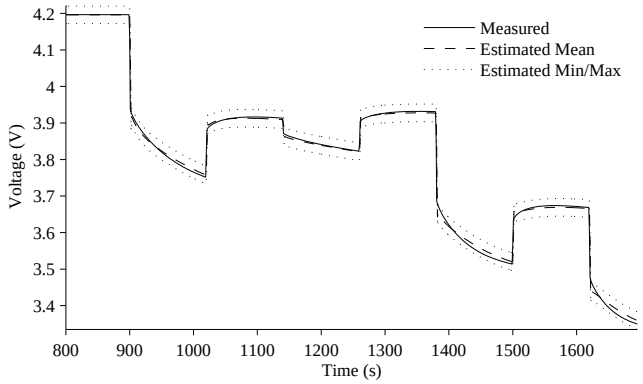

(a) Voltage estimation.

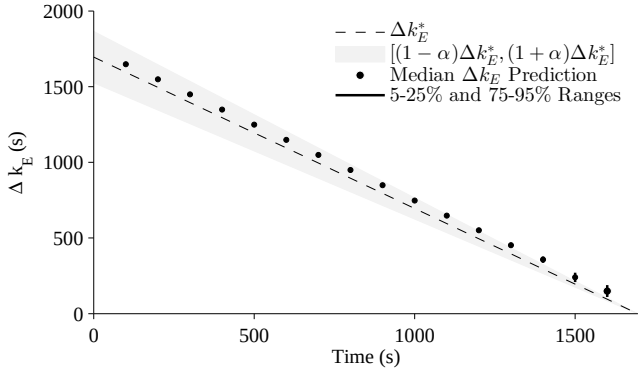

(b) EOD prediction

Figure 15. Prognostics results for variable loading discharge.

Table 3. Prognostics Performance

i_{app}	PRMSE	$\overline{\text{RA}}$	$\overline{\text{RMAD}}_{RUL}$
1.0	0.19	92.77	1.07
1.5	0.17	96.02	0.88
2.0	0.17	99.38	0.75
2.5	0.26	97.75	0.82
3.0	0.41	96.08	0.92

rate and efficient. As a result, prognostics results for EOD prediction are very accurate, with the uncertainty associated with the model remaining very small. Such a model has uses in other areas as well, such as control.

The model described here can also be applied to prognostics of battery packs. There are two approaches here: either each battery is modeled individually, or the batteries of the pack are lumped into an equivalent single-cell model. In the latter case, the prognostics framework as described here applies directly. In the former case, T_E must be redefined on a system-level (Daigle, Bregon, & Roychoudhury, 2012), such that the battery pack is said to be at EOD (or EOL) when any single battery in the pack is at EOD (or EOL).

The current model is limited in several ways that provide the basis for future work. For one, we have not described how the internal battery temperature changes over time. This is important because many of the potentials in the battery are functions of temperature. Further, diffusion rates should be impacted by temperature. Although we have described how aging can be represented within the model, we do not yet have descriptions of how these age-related parameters change over time, i.e., we require damage progression equations. Much work has already been done in this area but not with prognostics requirements and applications in mind. With such models, accurate end-of-life predictions can be made. Upon adding these missing elements, application of this modeling framework to different battery chemistries is also of interest.

ACKNOWLEDGMENT

This work was funded in part by the NASA System-wide Safety Assurance Technologies (SSAT) project under the Aviation Safety (AvSafe) Program of the Aeronautics Research Mission Directorate (ARMD), by the NASA Automated Cryogenic Loading Operations (ACLO) project under the Office of the Chief Technologist (OCT) of Advanced Exploration Systems (AES), and by the Advanced Ground Systems Maintenance (AGSM) Project under the Ground Sys-

tems Development and Operations program. The authors also acknowledge Brian Bole, Georgia Institute of Technology, for obtaining experimental data.

REFERENCES

Ceraolo, M. (2000, November). New dynamical models of lead-acid batteries. *IEEE Transactions on Power Systems*, *15*(4), 1184–1190.

Chen, M., & Rincon-Mora, G. (2006, June). Accurate electrical battery model capable of predicting runtime and I-V performance. *IEEE Transactions on Energy Conversion*, *21*(2), 504 - 511.

Daigle, M., Bregon, A., & Roychoudhury, I. (2012, September). A distributed approach to system-level prognostics. In *Annual conference of the prognostics and health management society* (p. 71-82).

Daigle, M., & Goebel, K. (2013, May). Model-based prognostics with concurrent damage progression processes. *IEEE Transactions on Systems, Man, and Cybernetics: Systems*, *43*(4), 535-546.

Daigle, M., Saha, B., & Goebel, K. (2012, March). A comparison of filter-based approaches for model-based prognostics. In *Proceedings of the 2012 IEEE aerospace conference.*

Daigle, M., Saxena, A., & Goebel, K. (2012, September). An efficient deterministic approach to model-based prediction uncertainty estimation. In *Annual conference of the prognostics and health management society* (p. 326-335).

Doyle, M., Fuller, T. F., & Newman, J. (1993, June). Modeling of galvanostatic charge and discharge of the lithium/polymer/insertion cell. *Journal of the Electrochemical Society*, *140*(6), 1526-1533.

Julier, S. J., & Uhlmann, J. K. (1997). A new extension of the Kalman filter to nonlinear systems. In *Proceedings of the 11th international symposium on aerospace/defense sensing, simulation and controls* (pp. 182–193).

Julier, S. J., & Uhlmann, J. K. (2004, mar). Unscented filtering and nonlinear estimation. *Proceedings of the IEEE*, *92*(3), 401–422.

Karthikeyan, D. K., Sikha, G., & White, R. E. (2008). Thermodynamic model development for lithium intercalation electrodes. *Journal of Power Sources*, *185*(2), 1398–1407.

Lee, K. J., Smith, K., Pesaran, A., & Kim, G. H. (2013, November). Three dimensional thermal-, electrical-, and electrochemical-coupled model for cylindrical wound large format lithium-ion batteries. *Journal of Power Sources*(1), 20-32.

Newman, J., & Tiedemann, W. (1975). Porous-electrode theory with battery applications. *AIChE Journal*, *21*(1), 25-41.

Ning, G., & Popov, B. N. (2004). Cycle life modeling of lithium-ion batteries. *Journal of The Electrochemical Society*, *151*(10), A1584–A1591.

Rahn, C. D., & Wang, C.-Y. (2013). *Battery systems engineering*. Wiley.

Ramadesigan, V., Northrop, P. W., De, S., Santhanagopalan, S., Braatz, R. D., & Subramanian, V. R. (2012). Modeling and simulation of lithium-ion batteries from a systems engineering perspective. *Journal of The Electrochemical Society*, *159*(3), R31–R45.

Rong, P., & Pedram, M. (2006). An analytical model for predicting the remaining battery capacity of lithium-ion batteries. *Very Large Scale Integration (VLSI) Systems, IEEE Transactions on*, *14*(5), 441–451.

Ross, P. (2013). Boeing's battery blues. *IEEE Spectrum*, *50*(3), 11-12.

Saha, B., & Goebel, K. (2009, September). Modeling Li-ion battery capacity depletion in a particle filtering framework. In *Proceedings of the annual conference of the prognostics and health management society 2009.*

Sankararaman, S., Daigle, M., Saxena, A., & Goebel, K. (2013, March). Analytical algorithms to quantify the uncertainty in remaining useful life prediction. In *Proceedings of the 2013 IEEE aerospace conference.*

Saxena, A., Celaya, J., Saha, B., Saha, S., & Goebel, K. (2010). Metrics for offline evaluation of prognostic performance. *International Journal of Prognostics and Health Management*, *1*(1).

BIOGRAPHIES

Matthew Daigle received the B.S. degree in Computer Science and Computer and Systems Engineering from Rensselaer Polytechnic Institute, Troy, NY, in 2004, and the M.S. and Ph.D. degrees in Computer Science from Vanderbilt University, Nashville, TN, in 2006 and 2008, respectively. From September 2004 to May 2008, he was a Graduate Research Assistant with the Institute for Software Integrated Systems and Department of Electrical Engineering and Computer Science, Vanderbilt University, Nashville, TN. From June 2008 to December 2011, he was an Associate Scientist with the University of California, Santa Cruz, at NASA Ames Research Center. Since January 2012, he has been with NASA Ames Research Center as a Research Computer Scientist. His current research interests include physics-based modeling, model-based diagnosis and prognosis, simulation, and hybrid systems. Dr. Daigle is a member of the Prognostics and Health Management Society and the IEEE.

Chetan S. Kulkarni received the B.E. (Bachelor of Engineering) degree in Electronics and Electrical Engineering from University of Pune, India in 2002 and the M.S. and Ph.D. degrees in Electrical Engineering from Vanderbilt University, Nashville, TN, in 2009 and 2013, respectively. In 2002 he joined Honeywell Automation India Limited (HAIL)

as a Project Engineer. From May 2006 to August 2007 he was a Research Fellow at the Indian Institute of Technology (IIT) Bombay with the Department of Electrical Engineering. From Aug 2007 to Dec 2012, he was a Graduate Research Assistant with the Institute for Software Integrated Systems and Department of Electrical Engineering and Computer Science, Vanderbilt University, Nashville, TN. Since Jan 2013 he has been a Research Engineer II with SGT Inc. at the Prognostics Center of Excellence, NASA Ames Research Center. His current research interests include physics-based modeling, model-based diagnosis and prognosis focused towards electrical and electronic devices and systems. Dr. Kulkarni is a member of the Prognostics and Health Management (PHM) Society, AIAA and the IEEE.